Title

Water-Surface Drag Coating: A New Route Toward High-Quality Conjugated Small-Molecule Thin Films with Enhanced Charge Transport Properties

Journal

Advanced Materials, 33(5)

ISSN

0935-9648

Authors

Deng, Wei
Xiao, Yanling
Lu, Bei
et al.

Publication Date

2021-02-01

DOI

10.1002/adma.202005915

Peer reviewed

Water-Surface Drag Coating: A New Route Toward High-Quality Conjugated Small-Molecule Thin Films with Enhanced Charge Transport Properties

Authors: Wei Deng[1], Yanling Xiao[1], Bei Lu[1], Liang Zhang[1], Yujian Xia[1], Chenhui Zhu[2], Xiujuan Zhang[1], Jinghua Guo[2], Xiaohong Zhang[1], and Jiansheng Jie[1]*,

Affiliations:

[1]Institute of Functional Nano & Soft Materials (FUNSOM), Jiangsu Key Laboratory for Carbon-Based Functional Materials & Devices, Soochow University, Suzhou, Jiangsu 215123, P. R. China

[2]Advanced Light Source, Lawrence Berkeley National Laboratory, Berkeley, CA 94720, USA

*Correspondence: jsjie@suda.edu.cn, xiaohong_zhang@suda.edu.cn

Abstract: Electronic properties of organic semiconductor (OSC) thin films are largely determined by their morphology and crystallinity. However, solution-processed small-molecule OSC thin films usually exhibit many grain boundaries as well as impure grain orientations because of complex fluid dynamics during solution coating. Here, we report a universal approach, water surface drag coating (WSDC), that relies on the water surface to alter the evaporation dynamics of solution for enlarging the grain size, and uses a unique drag-coating process to achieve the unidirectional epitaxial growth of the organic crystals. Using the WSDC, 2,8-Difluoro-5,11-bis(triethylsilylethynyl)anthradithiophene (Dif-TES-ADT) thin films with millimeter-sized single-crystalline domains and pure crystallographic orientations are achieved. As a result, carrier mobility of the Dif-TES-ADT thin films shows over 400% enhancement than that of conventional solution-coated thin films. The WSDC method

offers a facile route to enhance the charge transport properties of OSC thin films toward high-performance, large-area flexible electronics application.

Introduction

Organic field-effect transistors (OFETs) have attracted significant attention because they serve as fundamental building blocks for next-generation, flexible, and wearable electronics[1-4]. Among organic semiconductors (OSCs), small-molecule OSCs are especially interesting since they have traditionally led the field in terms of high-performance devices[5]. Significant efforts in the past decade have been made in molecular design and synthesis of new small-molecule OSCs with optimized molecular packing[6-11], which has led to the mobility of OFETs over 10 $cm^2 V^{-1} s^{-1}$, on par with polycrystalline silicon and metal oxide. While, in practice, their OFET performance is sensitively affected by the morphology and crystallinity of the thin films, especially grain boundaries and crystal orientations[12-15]. Grain boundaries and nonuniform crystal orientations will create charge transport barriers, exerting adverse effects on the electronic properties[16,17].

Meniscus-guided coating (MGC), such as dip coating, blade coating, solution shearing, and zone casting, has been recognized as a useful technique for the fabrication of OSC thin films with improved crystallinity and crystal orientations[12,18-25] because it makes use of a unidirectional force to guide the growth of grains in OSC thin films[12,20]. However, these thin films still exhibit many grain boundaries in the lateral direction and impure crystal orientations[12,13]. The grain boundaries orthogonal to the contact line are usually caused by the transversal depinning of solution due to the limited wettability of the solution on the substrate[26-29]. Plenty of carrier trapping centers arised from these grain boundaries will impair the charge transport properties

of the OSC thin films[30,31]. Also, motorial meniscus in the conventional MGC methods could cause a shearing fluid flow inside the solution and thereby induce a turbulent mass transport, which would lead to misaligned molecular packing and disordered crystal orientation. It would greatly hinder efficient charge transport[12,32-34] since the optimal charge transport direction is only along the strongest π orbitals overlap direction. It is worth noting that the limitation of nonuniform crystal orientation is not specific to the MGC methods, but is commonly observed in other solution-based methods as well. These disadvantageous fluid dynamics significantly affect the efficient charge transport of the OSC thin films prepared from the MGC methods. Therefore, it is in an urgent need to develop a new deposition strategy for OSC thin films, which can thoroughly alter the unfavourable fluid dynamics and thus improve the morphology and crystallinity of the resulting thin films.

Using water surface as a growth substrate has recently been demonstrated as a valid route for achieving OSC thin film with large-sized grains[35-38]. Water can help to enhance the wettability of organic solution on the growth substrates by facilitating the spreading of the solution on them. As a result, large-sized grains with remarkably reduced boundaries, especially in the lateral growth direction of the thin film, were achieved. Recent efforts have been devoted to further increase the grain sizes by regulating the properties of water[36,37]. While the lateral dimension of the grains can be improved to subcentimeter level[36], the area of obtained OSC thin films on the water surface is still less than ~0.1 cm^2, which is not sufficient for scalable device applications. It is most likely due to the limitation that all the reported water surface-

based approaches operate at molecular self-assembly process, where crystal growth is lack of the guidance of a continuous and unidirectional force like that in the MGC methods. It makes the self-assembled crystals can hardly grow large, and, more importantly, the crystal orientation of the grains randomly distributed and usually uncontrolled[35,38]. As such, the reproducibility and uniformity of the devices are still far from expectation.

Herein, we report a versatile water surface drag coating (WSDC) method that can create uniaxially oriented OSC thin films with single-crystalline domains in the millimeter scale. The proposed method combines the merits of continuous lateral crystal growth at the water surface and uniaxially epitaxial growth directed by a drag-coating process in the longitudinal direction. The fluid flow dynamics in the drag-coating process are quite different from those in the conventional MGC methods. As a consequence, sizes of the grains in the OSC thin films are remarkably enlarged, along with the significant improvement of the order degree of the molecular packing. As a result, carrier mobility of 2,8-Difluoro-5,11-bis(triethylsilylethynyl)anthradithiophene (Dif-TES-ADT) thin films fabricated by WSDC method shows 400% enhancement than that of the conventional blade-coating method. Flexible OFETs based on the Dif-TES-ADT thin film exhibit record-high average and maximum mobilities of 9.82 ± 1.72 and 16.1 $cm^2 V^{-1} s^{-1}$, respectively. This progress makes this strategy potentially suitable for large-area manufacturing of flexible electronics based on small-molecule OSC thin films.

Results

WSDC method. Fig. 1a illustrates the WSDC method for large-area coating of uniaxially orientated OSC thin films. First, a drop of a mixed solution containing Dif-TES-ADT/toluene and amorphous insulating polymer polystyrene (PS) was slowly injected onto the water surface along the wall of the Teflon water tank (Fig. 1a-i). The solution spread quickly across the water surface, forming a discrete OSC/polymer film with the evaporation of toluene. Then we utilized it as a sacrificial film for the subsequent growth of OSC thin film. When we continued to add the mixed solution, their spreading was observed to be blocked by the sacrificial film. These solutions were temporarily stored at the edge of the tank (Fig. 1a-ii). Then, we used a thin glass bar to drag the sacrificial films, as shown in Fig. 1a-iii, the stored solution started to spread again on the water surface. Computational fluid dynamics (CFD) simulation also verifies the above spreading process of the solution on the water surface (Fig. 1b and Movie S1). With the stored solution continuous spreading, the OSC thin film gradually grew out along the drag direction of the sacrificial film. The formed OSC thin film could cover the entire water surface with the area as large as 63 cm^2, as presented in Supplementary Fig. 1. Since the thin film formed on the water surface, it could be readily transferred onto a variety of target substrates, including SiO_2/Si substrate, paper, and polyethylene terephthalate (PET) (Supplementary Fig. 2). Fig. 1c displays the photograph of the highly uniform Dif-TES-ADT thin film obtained on a 2-inch PET substrate. Polarized optical microscopy (POM) image reveals that the Dif-TES-ADT thin film comprises large-sized grains, and the film has almost no grain

boundaries and structural defects in the millimeter-scale region. The Dif-TES-ADT grain in the thin film shows a consistent color when the growth direction of the thin film (dragging direction) is 45° relative to the polarisers' axes (Fig. 1d). However, when the growth direction is parallel to the axis of the crossed polarizers, the whole grain becomes dark (Fig. 1e). Such variation of POM images implies that the Dif-TES-ADT crystal domain possesses single-crystalline nature. Moreover, the wide and length of the single-crystalline domain can be extended to millimeter scale (Supplementary Fig. 3). In contrast, thin films produced by conventional blade-coating method show either dendritic/faceted grains separated by narrow gaps at low coating speed or a high density of grain boundaries separated by spherulitic crystals at a high coating speed (Supplementary Fig. 4). These phenomena could also be observed under other fabrication conditions in the blade-coating method, *e.g.*, concentration, temperature, and solvent (Supplementary Figs. 4-6). These comparative studies suggest that the WSDC method can significantly reduce the grain boundaries of the resulting Dif-TES-ADT thin film and thus enlarge the corresponding crystal grain sizes. Atomic force microscopy (AFM) displays the laminal morphology of the Dif-TES-ADT thin film (Fig. 1i); the step height of the lamellar crystal is about 1.6 nm, which is consistent with the thickness of the Dif-TES-ADT monolayer[39]. This is also a typical characteristic of layer-by-layer growth mode of OSCs[40,41], where molecules laterally grow until they coalesce into a continuous thin film, and then additional molecules start to grow upon the pre-formed thin film and eventually form lamellar crystals.

The introduction of a high-viscosity PS into Dif-TES-ADT/toluene solution can ensure the stable spreading of Dif-TES-ADT on the water surface and yield uniform OSC thin films (see detailed discussion below). Meanwhile, the addition of PS will not affect the crystallization behavior of Dif-TES-ADT molecules, because vertical phase separation would occur in the mixed solution during the spreading process[19,21,42]. To verify the vertical phase separation between Dif-TES-ADT and PS, the obtained thin film was examined by cross-sectional transmission electron microscopy (TEM). The sample was protected by an Au layer and then microtomed into ~450-nm thick slice by using a focused ion beam. In low-magnification cross-sectional TEM view (Fig. 1i, left), a 66-nm thick PS thin film with bright color can be easily observed due to its low crystallinity and electron density. An additional dark layer with ~4.8 nm thickness could also be visible between the Au layer and the PS layer in a high-magnification cross-sectional TEM image, which can be attributed to the Dif-TES-ADT thin film (Fig. 1i, right).

Our WSDC method also shows broad applicability to many widely used organic semiconductor molecules, including *p*-type 2,7-didecylbenzothienobenzothiophene (C_8-BTBT) and *n*-type 6,13-bis((triisopropylsilyl)ethynyl)-5,7,12,14-tetraazapentacene (TIPS-TAP). Supplementary Fig. 7 shows the orientated C_8-BTBT and TIPS-TAP thin films with large-sized single-crystalline domains. Moreover, compared with the corresponding blade-coated thin films, the grain size and the orientation of the drag-coated thin films are also significantly improved by using the WSDC method.

Crystallinity characterization. Fig. 2a shows the grazing-incidence wide-angle X-ray scattering (GIWAXS) pattern for the Dif-TES-ADT thin film prepared by the WSDC method. The thin film was transferred from the water surface to the SiO_2/Si substrate for detection. For comparison, Dif-TES-ADT thin film was also prepared on the SiO_2/ Si substrate by the conventional blade-coating method. Note that the Dif-TES-ADT thin film prepared by the WSDC method exhibits a first-order out-of-plane scattering point at q_z = 0.39 Å^{-1}, which is in good agreement with the (001) plane spacing of the Dif-TES-ADT crystal. This suggests that the Dif-TES-ADT molecules in the thin film have a stand-up orientation with respect to the substrate. In addition, the two intense in-plane scattering signals, appearing vertically at a given q_{xy}, can be indexed to {0, 1} and {1, 1}, respectively. The multiple in-plane spots suggest that our Dif-TES-ADT thin film consists of large-sized grains. In sharp contrast, the blade-coated Dif-TES-ADT thin film produces diffuse intensities around both the out-of-plane and in-planed diffraction peaks along the Debye rings, which indicates that the crystal domains are not well aligned in the blade-coated thin film. Based on these GIWAXS data, it can be concluded that the crystallographic orientation of the Dif-TES-ADT thin film is significantly improved by using the WSDC method. By comparing the scattering signals from different incident X-ray directions, the dominant crystal growth axis can be deduced. When the incident X-ray beams are perpendicular to the crystal growth direction (the drag-coating direction), (01*l*) diffractions related to *b* axis in the crystal lattice are observed. However, for the parallel incident X-ray beams, the intensities of (01*l*) diffractions are significantly weakened (Fig. 2c). The apparent discrepancy

manifests that crystal domains in the thin film have a uniaxial growth orientation along the *b* axis.

Crystallinity of the Dif-TES-ADT thin film is further examined by using select-area electron diffraction (SAED). The SAED patterns were randomly collected from three different regions in one crystal domain, which displayed a single set of diffraction spots of (100) and (010) crystal planes (Figs. 2d, e). This indicates the single-crystalline nature of the crystal domain and the fact that the Dif-TES-ADT thin film tends to grow horizontally along *ab*-plane and vertically along *c* axis. Identical diffraction patterns were observed from the other areas of the same crystal domain (Supplementary Fig. 8), suggesting that these crystal domains are single crystals with unitary crystallographic orientation. To further evaluate the molecular ordering inside the crystal domain, polarized Raman spectroscopy measurements were performed, as shown in Fig. 2f. The peaks located at 1374 and 1528/1578 cm^{-1} are associated with short- and long- axis vibrational modes along the conjugated backbone, respectively[43]. As the polarization angle of the incident laser aligns parallel to one of the two axes of the conjugated backbone, a maximum intensity of the Raman scattering signal is detected. With the polarization angle rotated by 360°, the intensities of the scattering signals associated with the long axis vibration of the molecule rise and fall periodically (Fig. 2g). This highly pronounced behavior evidences that the molecules inside the crystal domain are stacked orderly. Further structural information of the Dif-TES-ADT crystal domains was gained from high-resolution AFM. Crystal structure and lattice constants were extracted from Fast Fourier Transform of the AFM images

measured from 40 areas on the same crystal domain. Crystal structure of the Dif-TES-ADT thin film is determined to be triclinic with herringbone-type packing and lattice constants of a = 0.74 ± 0.15 nm, b = 0.76 ± 0.21 nm, and a = 73.3 ± 1.8° (Supplementary Figs. 9, 10), which is consistent with that of bulk crystals[39].

Enhancing the lateral growth of OSC thin film. In conventional MGC methods, solution wetting on a solid substrate (*e.g.*, SiO_2/Si) is usually partial and incomplete (Supplementary Fig. 11a); therefore, solution near the contact line would shrink, producing a "fingering-like" contact line (Figs. 3a, i, ii, and Supplementary Fig. 11b). This would cause molecular aggregation with uneven distributions, as shown in Fig. 3a-iii. As a result, the OSC thin films produced by the conventional MGC methods usually consisted of 1D dendritic crystals that were orthogonal to the receding contact line (Supplementary Figs. 4-6). In our WSDC method, water with high surface tension was used as the growth substrate. When organic solution with low surface tension was dropped on the water surface, surface tension gradients would cause spontaneous solution spreading, which is called surficial Marangoni flow (Fig. 3b-i). The surficial Marangoni flow could cause a complete wetting of organic solution on the water surface so that the solution contact line would be strongly pinned on the water surface. This could prevent fluid shrinking along the lateral growth direction (Fig. 3b-ii). In this case, the evaporation dynamics of the fluid was changed from "constant contact angle (CCA)" mode to "constant contact radius (CCR)" mode before crystallization. This CCR mode could effectively avoid the "coffee-ring" effect and facilitate a

homogenous distribution of molecules on the solution spreading area[44,45]. As a result, the lateral growth of OSC thin films was enhanced, which would substantially increase the size of single-crystalline domains and thus reduce the lateral grain boundaries (Fig. 3b-iii).

In order to have a deep insight into the lateral growth model, we investigated the morphologies of the thin films obtained from different concentrations of Dif-TES-ADT. Figs. 3c-e show the morphology evolution of the thin films with increasing the Dif-TES-ADT concentration in the solution. At a concentration below 0.8 mg mL^{-1}, discontinuous monolayer (ML) crystal domains, as shown in Fig. 3c, were obtained due to insufficient molecules supply. With the concentration increased to 1.2 mg mL^{-1}, the discontinuous crystals became coalesced and gradually grew into a continuous monolayer film. Notably, we also observed the next layer of crystals on the top of the Dif-TES-ADT monolayer (Fig. 3d). This scenario is well consistent with the lateral growth mode. Nevertheless, if we further increased the concentration to 2.0 mg mL^{-1} or more, many small grains with heavy thickness were observed on the top of the Dif-TES-ADT thin film (Fig. 3e), implying that the lateral growth mode has transformed to the upward island growth mode.

The enhanced lateral growth mode was further characterized by in-situ 2D grazing incidence X-ray diffraction (2D-GIXRD) (Figs. 3f-h). Weak diffraction pattern attributed to PS (Fig. 3g) was first detected when the mixed solution was dropped on water surface after 3s (t = 3s). This suggested that in the Dif-TES-ADT: PS blend solution, PS molecules first precipitated out due to its much lower solubility in toluene

than that of Dif-TES-ADT. With the toluene evaporated (t = 8s), two intense in-plane diffractions appeared, as shown in Fig. 3h, which can be indexed to be (014) and (113) planes of Dif-TES-ADT. The emergence of these diffractions indicated that Dif-TES-ADT crystals began to grow. Meanwhile, no diffraction spots were detected in the q_z (out-of-plane) direction. These results collectively confirm that in the beginning, the Dif-TES-ADT molecules preferentially grow along the in-plane direction and form monolayer thin film, which coincides with the lateral growth mode. After full evaporation of the solvent (t = 18s), multiple out-plane and in-plane diffraction spots appeared, indicating that the final obtained Dif-TES-ADT crystals consist of multi-stacked layers (Fig. 3i).

Epitaxial longitudinal growth of OSC thin films. The growth of Dif-TES-ADT thin film experiences three stages, as illustrated in Figs. 4a-c. After the formation of the sacrificial film, further added solution was stored at the tank edge, some of the Dif-TES-ADT molecules would precipitate out to form crystal nuclei at the contact line, and surficial Marangoni flow should have cause spontaneous solution spreading on the water surface. However, the existence of sacrificial film blocked their further motion, as shown in Fig. 4a. When the sacrificial film was dragging, the surficial flow would be retriggered, which would induce the stored solution to spread toward the contact line again and push the formed crystal nuclei to move. With the evaporation of the solution at the contact line, Dif-TES-ADT molecules would gradually precipitate out and crystallize at the nuclei *via* self-assembly. These deposited crystals would be

pulled away from the contact line with the dragging of the sacrificial film, as shown in Fig. 4b. If the dragging speed was very close to the crystallization rate, the precipitation and removal of the crystals could reach a balance, which could make the contact line maintain its original position during the crystal growth process (Supplementary Fig. 12). In this case, the location of the whole solution kept stationary, and the crystal growth occurred almost in a steady state. As the solvent evaporated, the evaporation-induced capillary flow would transport molecules unidirectionally to the contact line. Once these molecules were deposited out and grew along the nuclei at the contact line, they would be taken away immediately. With the sustained and stable molecular transport, continuous epitaxial growth of Dif-TES-ADT crystal occurred. It should be noted that the crystal growth was directed along the dragging direction, enabling the formation of uniaxially oriented OSC thin films (Fig. 4c). More importantly, no external forces were applied on the solution (the dragging force was applied on water and transmitted through the sacrificial film to make the crystal move); thus, the crystal growth was more like an equilibrium-state self-assembly process. Such epitaxial growth ensured the resulting thin films with high crystallinity and uniform orientation. In contrast, conventional MGC methods usually operate under non-equilibrium conditions, where external shear force is often imposed directly on the solution either by a coating head or by the substrate. The distribution of the shear forces inside the solution is uneven (Fig. 4d), which would cause turbulent and instable fluid flow, as shown in Fig. 4e. It has been reported that the unstable fluid flow within the solution could lead to disordered mass transport to the contact

line[12,33,46]. This would cause molecules irregularly aligned within the deposited crystals (Fig. 4f). Therefore, the degree of molecular orientations within the resulting thin films would be greatly reduced.

Next, we utilized Near-edge X-ray Absorption Fine-Structure (NEXAFS) Spectroscopy to further assess the molecular orientations in the thin films fabricated by the WSDC method and conventional MGC method (*e.g.*, blade coating at SiO_2/Si substrate), respectively. NEXAFS spectra were probed at different angular orientations with respect to the electric field polarization vector of the synchrotron light by rotating the samples. The geometry adopted in the measurements is illustrated in Fig. 4g. The morphologies of the as-prepared thin films were presented in the insets of Fig. 4h, i. In the NEXAFS spectra, the peaks located at 284-287 eV correspond to the transition from the C1s core-level to antibonding π^* orbitals of the conjugated backbone[42]. In the drag-coated thin film, the intensities of these peaks show significant rotation angular dependence (Fig. 4h). In particular, when the conjugated backbone planes were oriented perpendicular to the electric field (incident angle θ = 90°), a maximum intensity of the transition peaks was observed. While the intensity of these peaks became minimized when the electric field was oriented parallel to the conjugated backbone planes (θ = 20°). The above results show a well-oriented molecular packing inside the drag-coated Dif-TES-ADT thin film. While, the NEXAFS spectra for the blade-coated Dif-TES-ADT thin film showed very weak angle dependence, implying that molecules were weakly aligned inside the crystals (Fig. 4i). These results clearly manifest that the WSDC method can significantly improve the molecular packing

orientations in the resulting crystals.

Control experiments. Spreading coefficient (*S*) of the organic solution on the water surface plays a crucial role in our WSDC method. *S* is defined by the surface tensions at the contact line between a liquid droplet and substrate[47], where $S = \gamma_1 - \gamma_2 - \gamma_{12}$ (γ_1 and γ_2 are the surface tensions of water and the solution, respectively, and γ_{12} is the interfacial surface tension) (Supplementary Fig. 13a). When 1,2-dichlorobenzene (*o*-DCB) with a large γ_2 of 36.6 mN m^{-1} was used as the solvent, the *S* was -4.25 mN m^{-1}, thus the solution was observed to ball on the edge of the water tank[47], and aggregated crystals were eventually formed after solvent evaporation (Supplementary Figs. 13b, c). In order to realize the spontaneous spreading of the solution on the water surface, the solvent is normally required to have a relatively small γ_2 to make *S* positive. Thus, we chose toluene (γ_2 = 25 mN m^{-1}) as the solvent in the WSDC method, which was reported to have a postive *S* of 8.2 ± 1.2 mN m^{-1} [48]. As expected, Dif-TES-ADT/toluene was observed to have a good spontaneous spreading on water surface. Furthermore, *S* also decides the velocity of the surficial flow of the solution on the water surface. Since γ_1 is fixed and γ_2 is not influenced by the addition of PS (Supplementary Fig. 14), we changed the molecular weights (Mw) of PS to control γ_{12} to achieve the modulation of *S*. As shown in Supplementary Fig. 15, we plotted *S* as a function of the Mw of PS. When the Mw of PS varied from 925 to 2000 kDa, *S* showed an apparent decrease. When *S* was larger than ~13 mN m^{-1}, turbulent solution flow was observed on the water surface (Supplementary Figs. 16a-d), resulting in the

formation of small and disconnected crystal domains (Supplementary Figs. 16g, h). However, when PS with Mw higher than 925 kDa was used, *S* became relatively small, the flow on the water surface became steady as well (Supplementary Figs. 16e, f). Such stable surficial flow of solution can provide stable mass transport for molecular assembly, and thus promote long-range ordered crystallization of the OSC. As a result, high-quality crystalline thin films with uniaxial crystal orientations were achieved (Supplementary Figs. 16i, j). It can be seen that the Mw of PS strongly influences the stability of the surficial flow of solution on the water surface and thus the crystal quality and molecular orientations of the resulting thin films.

Morphologies and crystallization qualities of the resulting thin films fabricated by the WSDC method are also closely correlated with the dragging speed (Supplementary Fig. 17). If the dragging speed (e.g., 0.15 mm s^{-1}) was slower than the crystallization speed (V_c) of Dif-TES-ADT, the precipitated crystals could not be taken away in time, which would cause molecular aggregation at the contact line and eventually generate thicker films with small domains. If the dragging speed (e.g., 0.5 mm s^{-1}) was faster than the V_c, the solution around the contact line had not fully evaporated after the dragging, causing the pooling of solution on the water surface. Nonuniform crystallization would occur due to the "coffee-ring" effect. Only when the dragging speed (0.25 mm s^{-1}) was very close to the V_c, a continuous and smooth thin film with large single-crystalline domains could be achieved.

Charge transport properties and application on flexible OFETs. To assess the

charge transport properties of the resulting Dif-TES-ADT crystalline thin film, we transferred it onto a SiO_2/Si substrate and fabricated bottom-gate top-contact (BCBG) OFETs. Before electrical measurements, all the OFETs were patterned by mechanical scratches to avoid the fringe current. For comparison, OFETs based on the blade-coated thin films, which were prepared under different coating conditions, were also fabricated with the same device configuration. Fig. 5a depicts the typical transfer characteristics of a representative OFET based on the Dif-TES-ADT crystalline thin film fabricated from WSDC method. Significantly, the device exhibited a field-effect mobility (μ) as high as 15.3 $cm^2\ V^{-1}\ s^{-1}$ from the saturation region, along with a large on/off ratio of 1.45×10^7. In addition, the average mobility of 45 devices on the same substrate was calculated to be 10.1 ± 2.5 $cm^2\ V^{-1}\ s^{-1}$ (all devices are shown in Supplementary Fig. 18). In a sharp contrast, all of the OFETs based on the Dif-TES-ADT thin films perpared under various blade-coating conditions exhibited inferior device performance with a maximum average mobility of 2.14 $cm^2\ V^{-1}\ s^{-1}$ (Fig. 5b and Supplementary Fig. 19). A 470% increase of average mobility of OSC thin films was achieved (2.14 to 10.1 $cm^2\ V^{-1}\ s^{-1}$) through the WSDC method. Moreover, comparing with the mobility of the Dif-TES-ADT material in the previous reports[19,39,49-58], mobility of the Dif-TES-ADT thin film fabricated from WSDC method also shows a remarkable enhancement, reaching one of the best results of Dif-TES-ADT OFETs to date (Fig. 5c). The outstanding device performance of the drag-coated thin films was attributed to the reduced grain boundaries as well as the enhanced uniformity of molecular orientations in the crystals. The excellent device performance also testified

the superiority of the WSDC method.

Since the Dif-TES-ADT thin film was formed on water surface, it could be directly transferred onto any desired flexible substrate for device application. Fig. 5d shows the Dif-TES-ADT thin film-based flexible OFETs with a BCBG geometry, which composes of 50 nm Au as the source (S) and drain (D) electrodes, 310 nm SU-8 and 60 nm Al_2O_3 as gate dielectric layers, and 100 nm Al as gate electrodes. The typical channel width and length are 25 and 150 μm, respectively. The representative transfer and output characteristics of the device are shown in Figs. 5e, f. The μ extracted from the transfer characteristic in the saturation regime reaches as high as 16.1 cm^2 V^{-2} s^{-1}. It is observed that the device shows an outstanding linear transfer characteristic, which thus allows the most accurate mobility calculation. Meanwhile, the flexible OFET exhibits a large on-off current ratio of ~10^6, a small subthreshold slope of 0.78 V per decade, and a negligible V_T of -1.2 V. The negligible hysteresis and stable μ over a broad V_g range (Fig. 5g) reflect the high quality of the semiconductor-insulator interface and the absence of adverse effects from nonlinear contact resistance. Furthermore, 9 × 9 flexible OFET arrays were measured on the same substrate (Supplementary Fig. 20), yielding a high average and maximum μ of 9.82 ± 1.72 and 16.1 cm^2 V^{-2} s^{-1}, respectively (Fig. 5h). The maximum μ value is superior to the state-of-the-art flexible OFETs (Fig. 5i)[59-67], and the performance of flexible OFETs exceeds the benchmark mobility of 10 cm^2 V^{-2} s^{-1} for the first time. The remarkable improvement in flexible OFET performance has facilitated impressive application demonstrations, including high-resolution, flexible ultrahigh definition displays, high-

frequency radio frequency identification (RFID) tags, and high-speed flexible circuits[3,5]. It is noteworthy that the reported fabrication techniques for high-mobility OSC thin films are established on the rigid, flat and smooth substrates[12,19,23,42], which are very difficult to be migrated on the uneven flexible substrates. This is probably the main reason that the performance of the reported flexible OFETs is remarkably lower than that of the corresponding devices on the rigid substrates. However, in the WSDC method, the high-quality OSC thin films were prepared on water surface, thus removing the effect on the morphology and crystallinity of OSC thin films caused by the substrates. This guarantees that the high-performance flexible OFETs were achieved through WSDC.

Discussion

In conclusion, we have developed a versatile WSDC method that can obviously reduce the densities of grain boundary as well as improve the crystallization orientations of the resulting OSC thin films. As a result, uniaxial-orientation Dif-TES-ADT thin film with millimeter-scale single-crystalline domains was demonstrated, and over 400% enhancement of charge carrier mobility of the Dif-TES-ADT thin film was successfully achieved. GIWAXS and polarized Raman spectroscopy measurements verified the highly crystalline nature and ordered molecular packing inside the thin film. The thin film formation process had been systematically investigated by in situ GIXRD as well as the CFD simulation. Water surface could prevent the fluid shrinking along the lateral growth direction and gave rise to the

"CCR" mode of evaporation, which facilitated a homogenous lateral assembly of organic molecules and thus substantially reduced the lateral grain boundaries. In-situ GIXRD measurements confirmed the lateral growth model. Meanwhile, compared with the conventional MGC techniques, the drag coating process provided more stable molecule transport along the dragging direction; thus, continuous epitaxial longitudinal growth of crystals was successfully achieved under an equilibrium state. As a result, uniaxial-orientation Dif-TES-ADT thin film was attained. Synchrotron radiation NEXAFS measurements evidenced the much-improved degree of molecular packing order inside the drag-coated thin films than that of conventional blade-coated thin films. OFETs made from the Dif-TES-ADT thin films exhibited 4.7-fold improvement of the average carrier mobility (10.1 $cm^2 V^{-1} s^{-1}$) than that of the blade-coated Dif-TES-ADT thin films (2.14 $cm^2 V^{-1} s^{-1}$). Moreover, thin films fabricated by our method could be easily applied to fabricate flexible OFETs. An excellent carrier mobility of 16.1 $cm^2 V^{-1} s^{-1}$ was successfully attained for the Dif-TES-ADT thin films, which is among the highest for the flexible OFETs. Therefore, the proposed WSDC method is ideally suitable for the fabrication of high-quality OSC thin films with highly aligned crystalline domains toward flexible and high-performance organic electronics.

Methods

Materials. PS with different molecular weights were purchased from Sigma-Aldrich. Dif-TES-ADT, C_8-BTBT, and TIPS-TAP were purchased from Luminescence Technology Corp. and used as received without any further purification.

Fabrication of OSC thin films. All the small-molecule OSCs and PS were dissolved in toluene with a concentration of 10 mg mL^{-1}. The OSC and PS solutions were stirred for ~2 h before mixing them in 1:1 and 1:4 w/w ratio. First, 30 μL Dif-TES-ADT/PS mixed solution was slowly injected into the edge of the Teflon water tank. Subsequently, the pre-formed Dif-TES-ADT sacrificial layers were dragged by a bar at a constant velocity along a fixed direction. After that, Dif-TES-ADT thin film could cover the entire water surface. The brag speeds in the WSDC method explored range between 0.15 and 0.5 mm s^{-1}. For comparison, the blend solutions were blade coated using a set-up described in detail elsewhere. Blade coating was performed at wide speeds from 0.1 to 0.75 mm s^{-1} under different temperatures.

Characterizations of OSC thin films. The morphologies were characterized by a cross-polarized optical microscope (Olympus BX51) and AFM (Cypheres). For high-resolution AFM, the experiments were performed on an Asylum Cypher under ambient conditions using Asylum ARROW UHF AFM tips. The crystalline structures were further investigated by TEM (FEI, Tecnai G2 F20) and SAED operating at a 200 kV accelerating voltage. The GIWAXS were performed at Berkeley Lab's Advanced Light Source (ALS). The 2D-GIXRD measurements were performed at BL14B1 beamline (10 keV) at Shanghai Synchrotron Radiation Facility. NEXAFS measurements were performed at the bending magnet beamline 20A1 of the National Synchrotron Radiation Research Center (NSRRC), with a ring current of 500 mA. The NEXAFS resolution was set to 0.1 eV for carbon. A Horiba LabRAM HR coupled with a confocal microscope was used. A 633 nm laser source provided excitation for all the measurements, focused through a × 50 long working distance objective. The polarization of the monochromatic light was altered using a rotating quarter wavelength plate.

OFETs fabrication. Highly doped silicon wafers with 300-nm SiO_2 oxide layer were used as the substrates. The substrates were first scrubbed with a brush dipped in acetone and ultrasonicated in pure water, acetone, and isopropyl alcohol, respectively. Then these substrates were dried in the oven at 100°C. The OSC thin films obtained by the WSDC method were transferred on the SiO_2/Si substrates. Phase separation of the PS and the OSCs results in bilayer dielectric films (66-nm thick PS and 300-nm thick SiO_2), and the measured capacitance was about ~7.24 nF cm^{-2} (Supplementary Fig. 21). Finally, Au source and drain electrodes were thermally evaporated through a wire shadow mask with a channel length of 25 μm and a channel width of 150 μm, respectively. For the flexible device fabrication, an Al-covered PI substrate with a 60-nm thick Al_2O_3 and a 310-nm thick SU-8 double-layer dielectric was used. The measured capacitance was about ~6.49 nF cm^{-2} (Supplementary Fig. 22). Then the OSC thin films obtained on the WSDC method were transferred on the flexible substrates. Similarly, Au source and drain electrodes were thermally evaporated through a wire shadow mask with a channel length of 25 μm and a channel width of 150 μm, respectively. The electrical characterization was performed using a Keithley 4200-SCS semiconductor parameter analyzer.

Data availability

All the data supporting the findings in this study are available in the manuscript and in Supplementary Information. Further data and methods are available from the corresponding authors upon request.

References

1. Jiang, C. et al. Printed subthreshold organic transistors operating at high gain and ultralow power. *Science* **363**, 719-723 (2019).
2. Gumyusenge, A. et al. Semiconducting polymer blends that exhibit stable charge transport at high temperatures. *Science* **362**, 1131-1134 (2018).
3. Sirringhaus, H. 25th anniversary Article: organic field-effect transistors: the path beyond amorphous silicon. *Adv. Mater.* **26**, 1319-1335 (2014).

4. Duan, S. et al. Scalable fabrication of highly crystalline organic semiconductor thin film by channel-restricted screen printing toward the low-cost fabrication of high-performance transistor arrays. *Adv. Mater.* **31**, 1807975 (2019).

5. Mei, J. G., Diao, Y., Appleton, A. L., Fang, L. & Bao, Z. N. Integrated materials design of organic semiconductors for field effect transistors. *J. Am. Chem. Soc*. **135**, 6724-6746 (2013).

6. Liu, D. Q. et al. Self-assembled monolayers of phosphonic acids with enhanced surface energy for high-performance solution-processed n-channel organic thin-Film transistors. *Angew. Chem. Int. Ed*. **52**, 6222-6227 (2013).

7. Okamoto, T. et al. V-shaped organic semiconductors with solution processability, high mobility, and high thermal durability. *Adv. Mater.* **25**, 6392-6397 (2013).

8. Sokolov, A. N. et al. From computational discovery to experimental characterization of a high hole mobility organic crystal. *Nat. Commun.* **2**, 437 (2011).

9. Liu, Y. -Y. et al. High and balanced hole and electron mobilities from ambipolar thin-film transistors based on nitrogen-containing oligoacences. *J. Am. Chem. Soc*. **132**, 16349-16351 (2010).

10. Guo, X. G. et al. Bithiophene-imide-based polymeric semiconductors for field-effect transistors: synthesis, structure-property correlations, charge carrier polarity, and device stability. *J. Am. Chem. Soc*. **133**, 1405-1418 (2011).

11. Shi, Y Q. et al. Imide-functionalized thiazole-based polymer semiconductors: synthesis, structure-property correlations, charge carrier polarity, and thin-film transistor performance. *Chem. Mater.* **30**, 7988-8001 (2018).

12. Diao, Y. et al. Solution coating of large-area organic semiconductor thin films with aligned single-crystalline domains. *Nature Mater.* **12**, 665-671 (2013).

13. Deng, W. et al. Channel-restricted meniscus self-assembly for uniformly aligned growth of single-crystal arrays of organic semiconductors. *Mater. Today* **24**, 17-25 (2019).

14. Diao, Y., Shaw, L., Bao, Z. N. & Mannsfeld, S. C. B. Morphology control strategies for solution-processed organic semiconductor thin films. *Energy Environ.*

Sci. **7**, 2145-2159 (2014).

15. Zhou, Z. et al. Field-effect transistors based on 2D organic semiconductors developed by a hybrid deposition method. *Adv. Sci.* **6**, 1900775 (2019).
16. Ji, D. et al. Surface polarity and self-structured nanogrooves collaboratively oriented molecular packing for high crystallinity toward efficient charge transport. *J. Am. Chem. Soc.* **139**, 2734-2740 (2017).
17. Rivnay, J. et al. Large modulation of carrier transport by grain-boundary molecular packing and microstructure in organic thin films. *Nature Mater.* **8**, 952-958 (2009).
18. Chen, M., Peng, B., Huang, S. Y. & Chan, Paddy K. L. Understanding the meniscus-guided coating parameters in organic field-effect-transistor fabrications. *Adv. Funct. Mater.* **30**, 1905963 (2020).
19. Niazi, M. R. et al. Solution-printed organic semiconductor blends exhibiting transport properties on par with single crystals. *Nat. Commun.* **6**, 8598 (2015).
20. Janneck, R. et al. Predictive model for the meniscus-guided coating of high quality organic single-crystalline thin films. *Adv. Mater.* **28**, 8007-8013 (2016).
21. Zhang, K, et al. Crystallization control of organic semiconductors during meniscus-guided coating by blending with polymer binder. *Adv. Funct. Mater.* **28**, 1805594 (2018).
22. Li, L. Q. et al. Growth of ultrathin organic semiconductor microstripes with thickness control in the monolayer precision. *Angew. Chem. Int. Ed.* **52**, 12530-12535 (2013).
23. Yamamura, A. et al. Wafer-scale, layer-controlled organic single crystals for high-speed circuit operation. *Sci. Adv*.**4**, eaao5758 (2018).
24. Giri, G. et al. Tuning charge transport in solution-sheared organic semiconductors using lattice strain. *Nature* **480**, 504-508 (2011).
25. Sergi, R. -G., Adrian, T. & Marta, M. -T. Role of polymorphism and thin-film morphology in organic semiconductors processed by solution shearing. *ACS Omega*. **3**, 2329-2339 (2018).
26. Janneck, R. et al. Highly crystalline C_8-BTBT thin-film transistors by lateral

Homo-epitaxial growth on printed templates. *Adv. Mater.* **29**, 1703864 (2017).

27. Maheshwari, S., Zhang, L., Zhu, Y. X. & Chang, H. -C. Coupling between precipitation and contact-line dynamics: multiring stains and stick-slip motion. *Phys. Rev. Lett.* **100**, 044503 (2008).
28. Corrales, T. P. et al. Spontaneous formation of nanopatterns in velocity-dependent dip-coated organic films: from dragonflies to stripes. *ACS Nano* **8**, 9954-9963 (2014).
29. Huang, J. X., Kim, F., Tao, A. R., Commor, S. & Yang, P. Spontaneous formation of nanoparticle stripe patterns through dewetting. *Nat. Mater.* **4**, 896-900 (2005).
30. Choi, H. H. et al. Hall effect in polycrystalline organic semiconductors: the effect of grain boundaries. *Adv. Funct. Mater.* **29**, 1903617 (2019).
31. Chwang, A. B. & Frisbie, C. D. Temperature and gate voltage dependent transport across a single organic semiconductor grain boundary. *J. Appl. Phys.* **90**, 1342 (2001).
32. Gu, X. D. et al. The meniscus-guided deposition of semiconducting polymers. *Nat. Commun.* **9**, 534 (2018).
33. Park, K. S. et al. Tuning conformation, assembly, and charge transport properties of conjugated polymers by printing flow. *Sci. Adv.* **5**, eaaw7757 (2019).
34. Schott, S. et al. Charge-transport anisotropy in a uniaxially aligned diketopyrrolopyrrole-based copolymer. *Adv. Mater.* **27**, 7356-7364 (2015).
35. Xu, C. H. et al. A general method for growing two-dimensional crystals of organic semiconductors by "solution-epitaxy". *Angew. Chem. Int. Ed.* **55**, 9671-9675 (2016).
36. Wang, Q. Q. et al. Space-confined strategy toward large-area two-dimensional single crystals of molecular materials. *J. Am. Chem. Soc.* **140**, 5339-5342 (2018).
37. Yao, J. R. et al. Layer-defining strategy to grow two-dimensional molecular crystals on a liquid surface down to the monolayer limit. *Angew. Chem. Int. Ed.* **58**, 16082-16086 (2019).

36. Zhu, X. T. et al. 2D molecular crystal bilayer p-n junctions: a general route toward

high-performance and well-balanced ambipolar organic field-effect transistors. *Small* **15**, 1902187 (2019).

39. Jurchescu, O. D. et al. Organic single-crystal field-effect transistors of a soluble anthradithiophene. *Chem. Mater*. **20**, 6733-6737 (2008).

40. Huang, L. Z. et al. Tunable field-effect mobility utilizing mixed crystals of organic molecules. *Adv. Mater*. **23**, 3455-3459 (2011).

41. Heringdorf, F. -J. M., Reuter, M. C. & Tromp, R. M. Growth dynamics of pentacene thin films. *Nature* **412**, 517-520 (2001).

42. Yuan, Y. et al. Ultra-high mobility transparent organic thin film transistors grown by an off-centre spin-coating method. *Nat. Commun*. **5**, 3005 (2014).

43. Huang, C. -W. et al. Micro-raman imaging of isomeric segregation in small-molecule organic semiconductors. *Commun. Chem.* **2**, 22 (2019).

44. Barmi, M. R. & Meinhart, C. D. Convective flows in evaporating sessile droplets. *J. Phys. Chem. B* **118**, 2414-2421 (2014).

45. Zang, D. et al. Evaporation of a droplet: from physics to applications. *Phys. Rep.* **804**, 1-56 (2019).

46. Wang, Z., Ma, Z. & Li, L. B. Flow-induced crystallization of polymers: molecular and thermodynamic considerations. *Macromolecules* **49**, 1505-1517 (2016).

47. Noh, J., Jeong, S. & Lee, J. -Y. Ultrafast formation of air-processable and high-quality polymer films on an aqueous substrate. *Nat. Commun*. **7**, 12374 (2016).

48. Dussaud, A. D. & Troian, S. M. Dynamics of spontaneous spreading with evaporation on a deep fluid layer. *Phys. Fluids* **10**, 23 (1998).

49. Hamilton, R. et al. High-performance polymer-small molecule blend organic transistors. *Adv. Mater.* **21**, 1166-1171 (2009).

50. Smith, J. et al. Air-stable solution-processed hybrid transistors with hole and electron mobilities exceeding 2 $cm^2 V^{-1} s^{-1}$. *Adv. Mater.* **22**, 3598-3602 (2010).

51. Smith, J. et al. Percolation behaviour in high mobility p-channel polymer/small-molecule blend organic field-effect transistors. *Org. Electron.* **12**, 143-147 (2011).

52. Smith, J. et al. Solution-processed small molecule-polymer blend organic thin-film

transistors with hole mobility greater than 5 cm^2/Vs. *Adv. Mater.* **24**, 2441-2446 (2012).

53. Mei, Y. C. et al. High mobility field-effect transistors with versatile processing from a small-molecule organic semiconductor. *Adv. Mater.* **25**, 4352-4357 (2013).

54. Hunter, S. Chen, J. & Anthopoulos, T. D. Microstructural control of charge transport in organic blend thin-film transistors. *Adv. Funct. Mater*. **24**, 5969-5976 (2014).

55. Temiño, I. et al. A rapid, low-cost, and scalable technique for printing state-of-the-art organic field-effect transistors. *Adv. Mater. Technol*. **1**, 1600090 (2016).

56. Diemer, P. J. et al. The influence of isomer purity on trap states and performance of organic thin-film transistors. *Adv. Electron. Mater.* **3**, 1600294 (2017).

57. Panidi, J. et al. Remarkable enhancement of the hole mobility in several organic small-molecules, polymers, and small-molecule: polymer blend transistors by simple admixing of the lewis acid p-dopant $B(C_6F_5)_3$. *Adv. Sci*. **5**, 1700290 (2018).

58. Xiao, Y. L. et al. Surfcial marangoni flow-induced growth of ultrathin 2D molecular crystals on target substrates. *Adv. Mater. Interfaces* **7**, 1901753 (2019).

59. Briseno, A. L. *et al.* High-performance organic single-crystal transistors on flexible substrates. *Adv. Mater.* **18**, 2320-2324 (2006).

60. Sekitani, T., Zschieschang, U., Klauk, H. K. & Someya, T. Flexible organic transistors and circuits with extreme bending stability. *Nat. Mater*. **9**, 1015-1022 (2010).

61. Nakayama, K. *et al*. Patternable solution-crystallized organic transistors with high charge carrier mobility. *Adv. Mater.* **23**, 1626-1629 (2011).

62. Kaltenbrunner, M. et al. An ultra-lightweight design for imperceptible plastic electronics. *Nature* **499**, 458-463 (2013).

63. Fukuda, K. et al. Fully-printed high-performance organic thin-film transistors and circuitry on one-micron-thick polymer films. *Nat. Commun.* **5**, 4147 (2014).

64. Ji, D. Y. *et al*. Copolymer dielectrics with balanced chain-packing density and surface polarity for high-performance flexible organic electronics, *Nat. Commun*. **9**,

2339 (2018).

65. Huang, Y. *et al.* Scalable processing of low voltage organic field effect transistors with a facile soft-contact coating approach. *IEEE Electron Device Lett*. **40**, 1945-1948 (2019).

66. Guo, L. *et al*. Flexible semi-transparent organic transistors and circuits based on easily prepared polyphenyleneoxide dielectric. *Org. Electron.* **69**, 308-312 (2019).

67. Duan, S. M. *et al*. Solution-processed centimeter-scale highly aligned organic crystalline arrays for high-performance organic field-effect transistors. *Adv. Mater.* **32**, 1908388 (2020).

Acknowledgements

This work was supported by the National Natural Science Foundation of China (Grant Nos. 51973147, 61904117, 51821002 and 51672180), the Natural Science Foundation of Jiangsu Province of China (BK20180845), the Priority Academic Program Development of Jiangsu Higher Education Institutions (PAPD), the 111 Project, and Collaborative Innovation Center of Suzhou Nano Science and Technology (Nano-CIC). We thank the beamline BL14B1 (Shanghai Synchrotron Radiation Facility), BL7.3.3 (Advanced Light Source), and for BL20A1 (National Synchrotron Radiation Research Center) providing the beam time.

Author contributions

W.D. J.S.J. and X.H.Z. conceived and designed the experiments. W.D. X.J.Z. and Y.L.X. performed the experiments. L.Z. and Y.J.X. contributed to NEXAFS measurement and analysis. C.H.Z. and J.H.G. contributed to GIWAXS measurement and analysis. B.L. contributed to CFD simulation. W.D. J.S.J. X.J.Z. and X.H.Z. discussed the results and co-wrote the manuscript.

Competing financial interests

The authors declare no competing financial interests.

Figures and captions

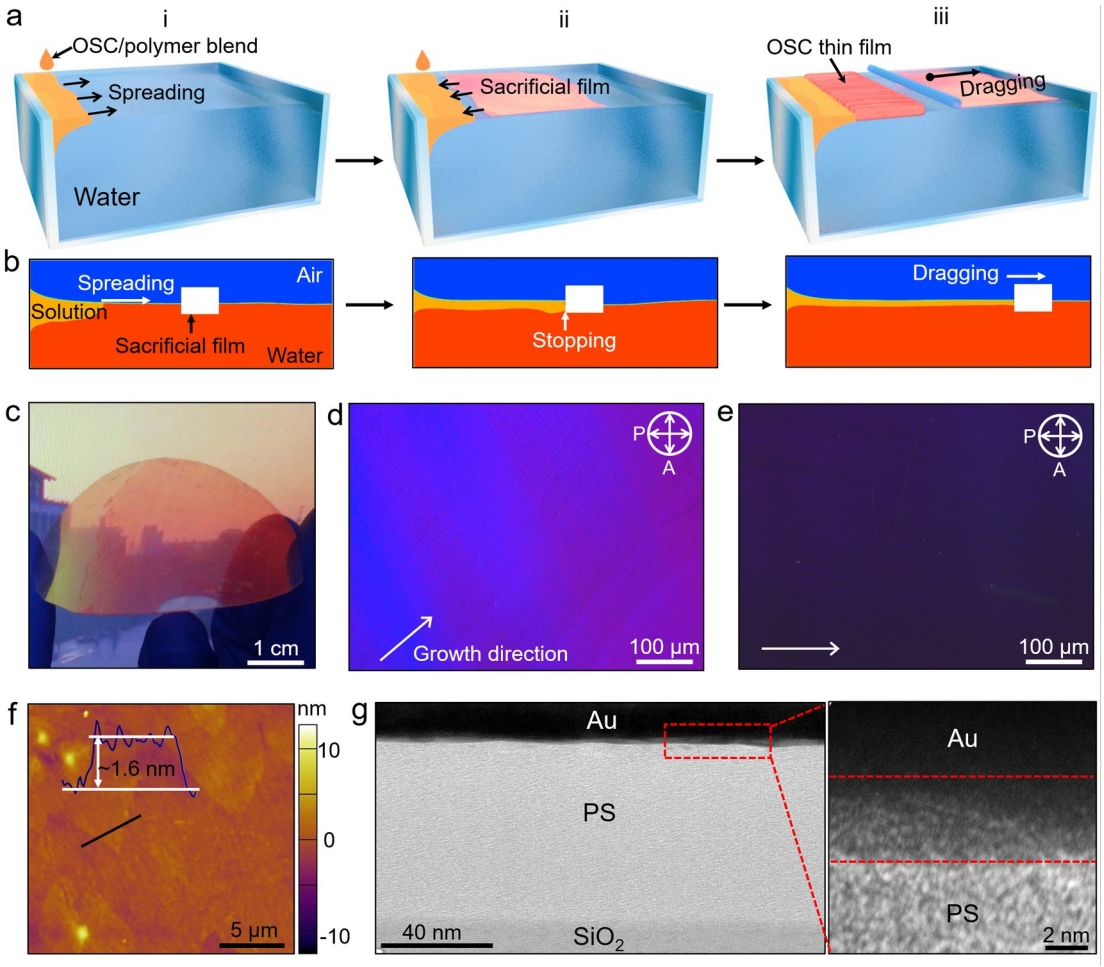

Fig. 1 Dif-TES-ADT thin films fabricated by WSDC method. (**a**) Schematic diagram for the fabrication of OSC thin films by using the WSDC method. (**b**) CFD simulation of the spreading process of the solution on the water surface. (**c**) Transferred Dif-TES-ADT thin film on a 2-inch PET substrate. (**d**, **e**) POM images of the Dif-TES-ADT thin film fabricated from the WSDC method. The crossed arrows indicate the orientations of crossed polarizers. (**f**) AFM image of the Dif-TES-ADT thin film. Inset: height profile along the black line. (**g**) Cross-sectional TEM image of the resulting Dif-TES-ADT thin film.

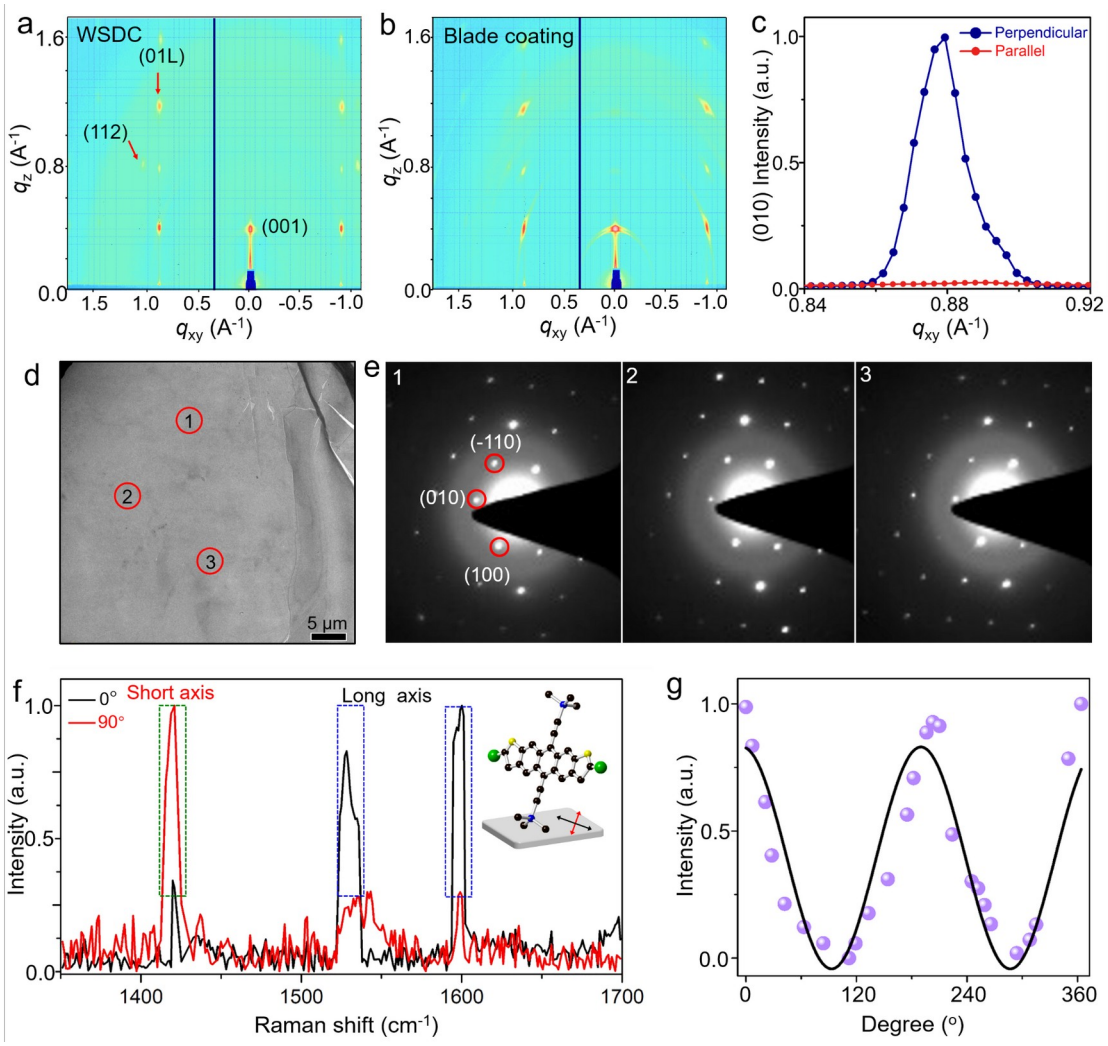

Fig. 2 Characterizations of the crystalline quality of the Dif-TES-ADT thin film. GIWAXS images of the Dif-TES-ADT thin film fabricated from (**a**) WSDC method and (**b**) conventional blade coating method. (**c**) In-plane XRD patterns for (010) peak detection with the X-ray perpendicular and parallel to the dragging direction. (**d**) TEM image of the crystal domain within the Dif-TES-ADT thin film and (**e**) its corresponding SAED patterns collected from different areas. (**f**) Raman spectra captured under different polarization angles (0° and 90°). (**g**) Intensities of the long axis vibration (1528 cm^{-1}) of the Dif-TES-ADT molecule *versus* the polarization angles.

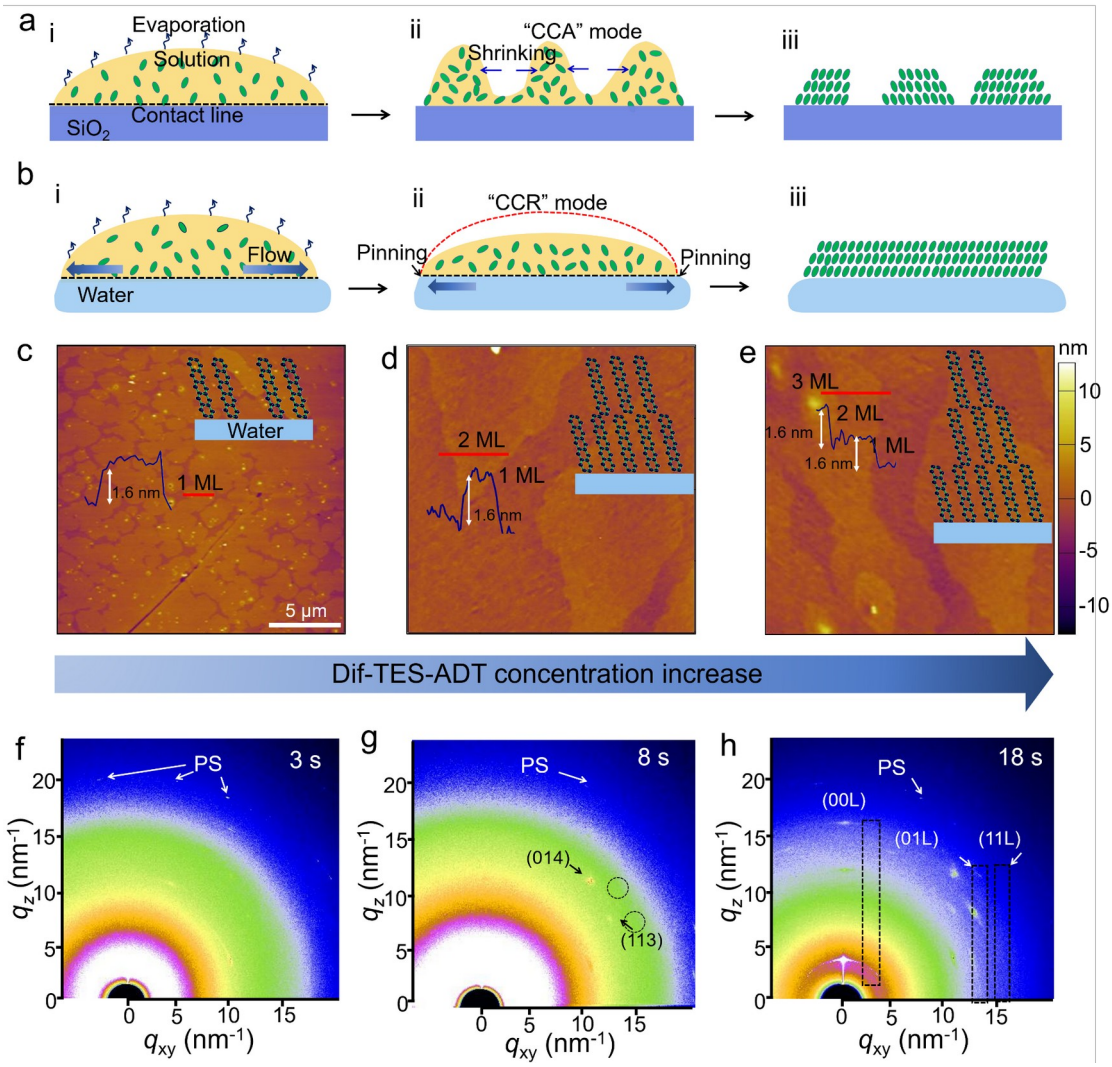

Fig. 3 Lateral growth mode of the Dif-TES-ADT thin film on the water surface. Schematic illustrations of molecule assembly on the (**a**) SiO_2/Si substrate and (**b**) water surface. (**c-e**) AFM images of the morphology evolution of the Dif-TES-ADT thin film with increasing the Dif-TES-ADT concentration. From left to right, the Dif-TES-ADT solution concentrations are 0.8, 1.2, and 2 mg mL^{-1}, respectively. (**f-h**) In-situ GIXRD measurement performed during the drying process of Dif-TES-ADT: PS blend solution.

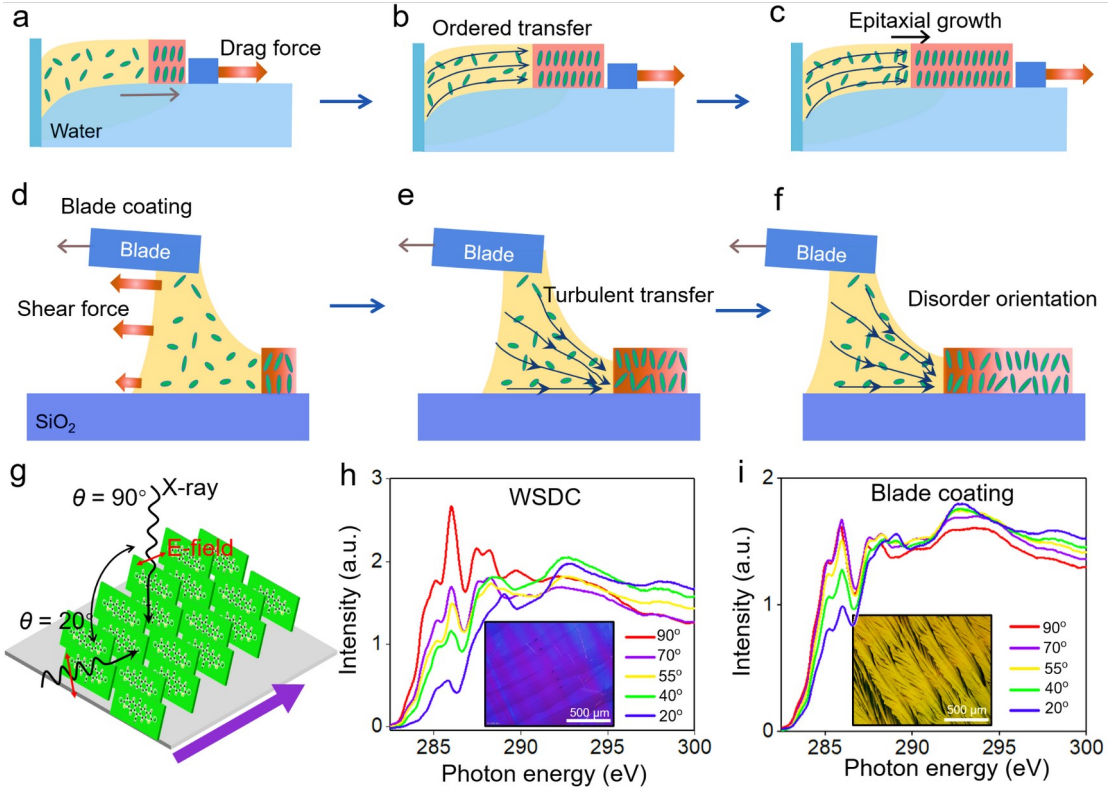

Fig. 4 Orientated growth of OSC thin films. (**a-c**) Schematic illustration of the formation of Dif-TES-ADT thin film during the dragging process. (**d-f**) Schematic illustration of the formation of Dif-TES-ADT thin film through blade coating. The arrows indicate the mass transport. (**g**) Schematic illustration of geometry adopted for the NEXAFS measurements. θ denotes the angle of the incident X-ray. Carbon K edge NEXAFS spectra for the Dif-TES-ADT thin films prepared from (**h**) WSDC method and (**i**) blade-coating method at different θ angles. Insets show POM images of the Dif-TES-ADT thin films prepared from the WSDC method and blade-coating method, respectively.

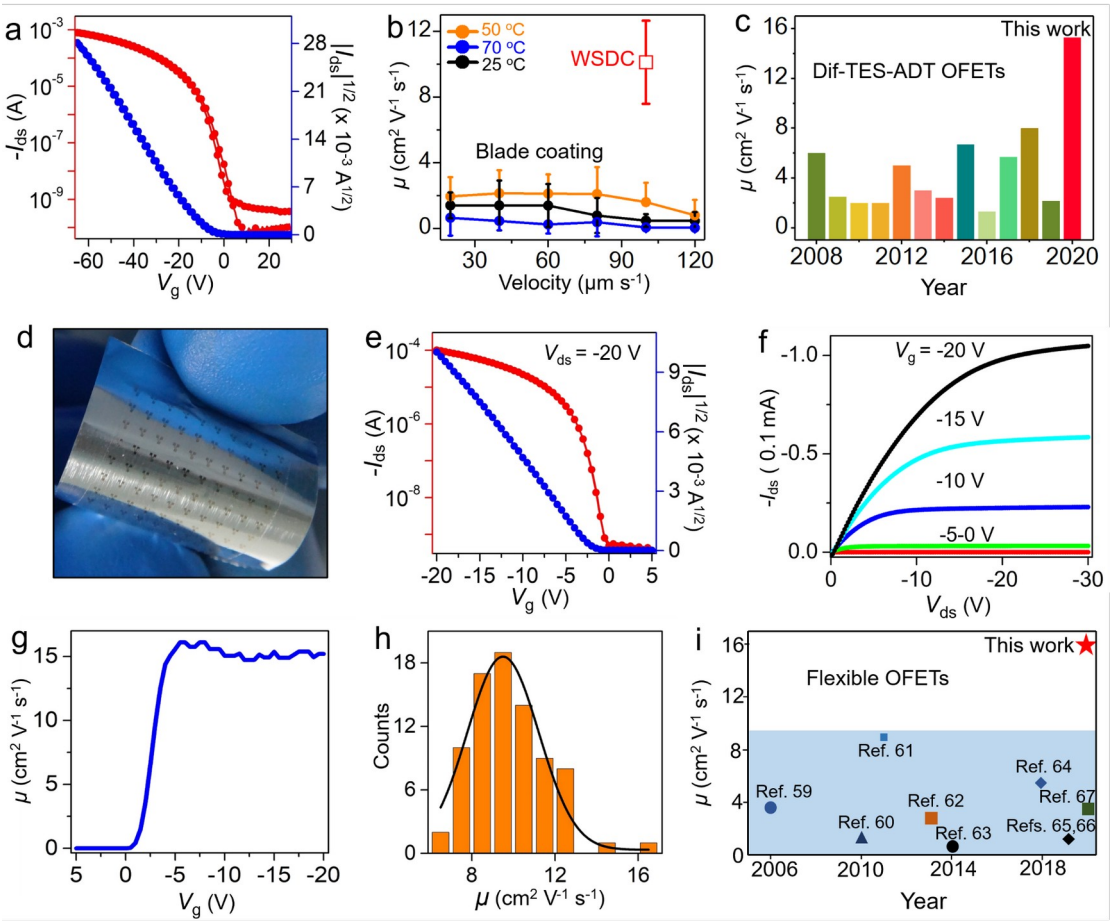

Fig. 5 Charge transport properties of the Dif-TES-ADT thin film grown by WSDC method and high-performance flexible OFETs. (**a**) Representative transfer characteristic of the Dif-TES-ADT thin film-based OFET prepared on the SiO_2/Si substrate. (**b**) Comparison of mobilities for Dif-TES-ADT thin films fabricated by the WSDC method and blade coating. (**c**) Comparing mobility of Dif-TES-ADT material of this work and references[19,39,49-58]. (**d**) Photograph of the flexible OFETs based on Dif-TES-ADT thin film prepared from the WSDC method. (**e**) Transfer and (**f**) output characteristics of the flexible OFET device, and (**g**) corresponding mobility *versus* gate voltage curve. (**h**) Mobility distribution of 81 flexible OFET devices on the same substrate. (**i**) Distribution of the maximum mobility of organic flexible OFETs in the references[59-67] and this work.